Unsteady crystal growth due to step-bunch cascading

Peter G. Vekilov, Hong Lin, and Franz Rosenberger*
Center for Microgravity and Materials Research, University of Alabama in Huntsville, Huntsville, Alabama 35899
(Received 30 August 1996)

Based on our experimental findings of growth rate fluctuations during the crystallization of the protein lysozyme [Vekilov, Alexander, and Rosenberger, Phys. Rev. **54**, 6650 (1996)], we have developed a numerical model that combines diffusion in the bulk of a solution with diffusive transport to microscopic growth steps that propagate on a finite crystal facet. Nonlinearities in layer growth kinetics arising from step interaction by bulk and surface diffusion, and from step generation by surface nucleation, are taken into account. On evaluation of the model with properties characteristic for the solute transport, and the generation and propagation of steps in the lysozyme system, growth rate fluctuations of the same magnitude and characteristic time, as in the experiments, are obtained. The fluctuation time scale is large compared to that of step generation. Variations of the governing parameters of the model reveal that both the nonlinearity in step kinetics and mixed transport-kinetics control of the crystallization process are necessary conditions for the fluctuations. On a microscopic scale, the fluctuations are associated with a morphological instability of the vicinal face, in which a step bunch triggers a cascade of new step bunches through the microscopic interfacial supersaturation distribution. [S1063-651X(97)14203-9]

PACS number(s): 81.10.Aj, 47.20.Bp, 68.35.Ct.

I. INTRODUCTION

The compositional and structural uniformity of a crystal is largely determined by the dynamics of molecular layer (growth step) spreading. Unsteady layer propagation and step bunching are often associated with nonuniform impurity trapping and lattice defect formation [1,2]. Most recently, we have presented experimental evidence for unsteady step dynamics during the crystallization of the protein lysozyme from aqueous solutions under steady external conditions [3]. Based on a scaling analysis, we concluded that the observed fluctuations originate from the coupling of bulk transport with nonlinear interface kinetics. Furthermore, these considerations suggest that fluctuations in step density may be a rather widespread phenomenon in crystallization. In inorganic systems, however, only a few observations of unsteady growth, that are possibly the result of the nonlinear interaction between bulk transport and interface kinetics, have been reported [4–7]. In protein crystallization, growth steps are higher and their kinetics are typically slower [8] than in inorganic systems [9]. Thus, growth unsteadiness may be more readily detectable even with the spatial-temporal resolution limits of current observation techniques.

In this work we test the supposition that the observed fluctuations root in the coupling between bulk transport and nonlinear interface kinetics. Retaining the essential geometry of our experiments, we develop a two-dimensional (2D) model for the diffusive transport from the bulk of a solution to microscopic growth steps on a faceted crystal. Both stochastic and deterministic step generation through surface nucleation are employed. The step spreading velocity is assumed to depend on both the local supersaturation and step density. We evaluate this model for transport, kinetics and step generation parameters characteristic of lysozyme. This results in growth rate fluctuations of the same magnitude and characteristic time as in our experiments. On increase of the bulk diffusivity (shift towards kinetically controlled growth), the model yields relatively steady step dynamics. However, a stronger interaction (surface diffusion field overlap) between steps, i.e., an increase in the nonlinearity of the step kinetics, results in a larger amplitude of the fluctuations. On a microscopic scale, we find that the unsteadiness is the result of a novel morphological instability, in which a cascade of step bunches forms in response to the perturbation in the interfacial supersaturation distribution introduced by existing bunches.

II. MODEL

A. Diffusive bulk transport

The geometry of the transport model is based on the setup used in our experimental investigations of nonlinear growth layer dynamics [3,10]. As depicted in Fig. 1(a), the crystallization cell is approximated by a 2D closed domain of 1 mm height and 6 mm width. A crystal of fixed size, 0.6 mm wide and 0.3 mm high, rests on the middle of the cell bottom. The model solution consists of the protein lysozyme (component 1) in water. The initial lysozyme mass concentration in the solution is $\rho_{1,0}=50$ mg/ml. At 12 °C, and the precipitant concentration and pH used in the experiments [3,10,11], the solubility of lysozyme is $\rho_1^{eq}=3.1$ mg/ml [12]. Hence, the initially uniform value of the supersaturation $\sigma=\ln(\rho_1/\rho_1^{eq})$ is $\sigma_0=2.78$.

We consider only diffusive transport of a dilute solute. Thus, the conservation equation for lysozyme in the solution is

$$\frac{\partial \rho_1}{\partial t}=D_1\left(\frac{\partial^2 \rho_1}{\partial x^2}+\frac{\partial^2 \rho_1}{\partial z^2}\right), \tag{1}$$

*Corresponding author.

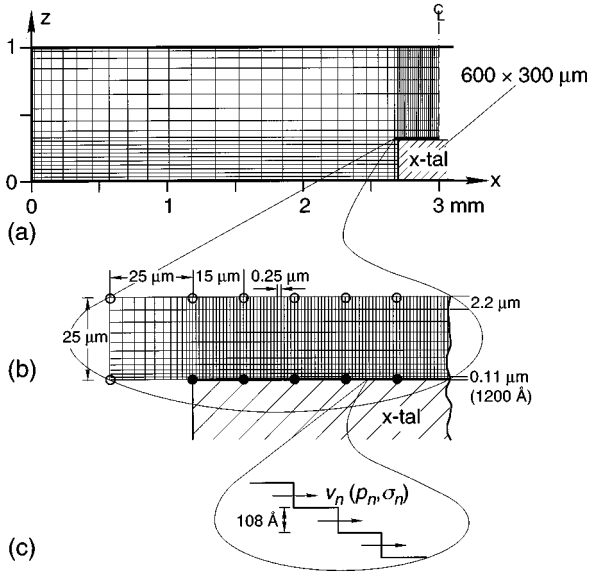

FIG. 1. Geometry and grids used in the simulations. (a) Bulk (global) mass transport, 45×21 grid, (b) interfacial (mesoscale) subdomain, 1221×21 grid, (c) steps moving in interface [heavy black line in (b)].

where the diffusivity is $D_1=1.06\times10^{-6}$ cm^2/s [13,14]. Furthermore, due to the symmetry of the transport problem,

$$\frac{\partial\rho_1}{\partial x}=0 \tag{2}$$

on the center line of the cell, including the interface. The walls of the cell are assumed to be impermeable, i.e., $\nabla\rho_1\cdot\mathbf{n}=0$, where $\mathbf{n}$ is normal to the wall.

The solution-crystal interface consists of singular terraces between microscopic growth steps. The initially uniform growth step density is given by the initial vicinal slope of the interface p_0 and the height of the growth steps h. With the typical values $p_0=5\times10^{-3}$ [3] and $h=108$ Å≈0.01 μm (unit cell dimension in the $\langle110\rangle$ direction [15]), about 140 equidistant steps initially cover the half facet. In view of these low values of p_0, we ignore, for the transport calculations, the actual vicinality of the interface and assume that the steps move within a singular horizontal interface, which is represented by the heavy horizontal line in Fig. 1(b). This simplification is well supported by scaling arguments. Local height differences in the interface morphology, as they may arise, e.g., from macrosteps of height mh (bunching of m elementary steps) result only in significant supersaturation differences in the z direction if the step velocity v in the bunch is significant compared to the characteristic diffusion velocity D_1/mh. Our experimental results (see, e.g., the local minima of $v(t)$, Fig. 9 in [3]) reveal that for lysozyme v in a bunch is of $O(10^{-5}$ cm/s), while $mh\leqslant5\times10^{-6}$ cm and, thus, the diffusion velocity about macrosteps is of $O(10^{-1}$ cm/s).

To resolve the concentration field about individual growth steps, we introduce a mesoscale (MS) subdomain above the interface, see Fig. 1(b) and Sec. III. The interfacial concentration boundary condition for the MS domain is tied to the protein consumption at the moving steps. If there are $N_{\rm sink}(i)$ steps within the ith mesh in the grid used for the numerical simulation in the MS domain, flux balance requires that

$$\sum_{N_{\rm sink}(i)} v(n)\rho_1^c h=D_1\left.\frac{\partial\rho_1}{\partial z}\right|_i\Delta x^{\rm MS}, \tag{3}$$

where $v(n)$ is the velocity of the nth step, $\rho_1^c=0.82$ g/cm^3 is the protein mass density in the lysozyme crystal [15], and $\Delta x^{\rm MS}$ is the mesh width. Due to the low mass fraction ρ_1/ρ (ρ: total mass density) of the protein in the solution, the above simple form of Fick's first law is adequate for the diffusive flux [16].

B. Step motion and step generation

As in our earlier work [8,17,18], we assume that the velocity of the steps follows the relation

$$v(n)=\frac{b_{\rm step}\sigma^s(n)}{1+kp(n)}=\frac{b_{\rm step}\ln[\rho_1^s(n)/\rho_1^{\rm eq}]}{1+kp(n)}, \tag{4}$$

where $b_{\rm step}$ is the step kinetics coefficient and $\sigma^s(n)$ is the interfacial supersaturation at the nth step, with ρ_1^s the protein mass density at step n and $\rho_1^{\rm eq}$ the bulk equilibrium concentration. The group $kp(n)$, with $p(n)$ the slope about the nth step, accounts for the mutual deceleration of adjacent steps through overlap of their surface diffusion fields. The stronger the competition for nutrient among neighboring steps, i.e., the larger $kp(n)$, the lower is $v(n)$; for details see [17]. Note that, in principle, $\rho_1^{\rm eq}$ and, thus, σ^s are subject to the local curvature of the interface. From a macroscopic point of view, this capillary effect is only significant if the radius of surface curvature is comparable to or smaller than $r^s=\Gamma/\sigma^s$, where $\Gamma=\Omega\alpha/k_BT$ is the capillary length, with Ω: the molecular volume in the crystal and α: the surface free energy [19,20]. As discussed in [3], due to the low value of α, Γ for lysozyme is of $O(100$ Å). With a typical σ^s of order unity, this suggests that capillary effects can be ignored down to radii of curvature which are comparable to the step height h in our model. A more realistic estimate of microscopic curvature effects, based on molecular interactions, will likely result in a somewhat larger length scale for capillary effects. However, as we will see in Sec. VI C, the smallest r^s's obtained on step bunching from our model exceed Γ by several orders of magnitude. Hence, the use of a constant $\rho_1^{\rm eq}$, independent of microscopic morphology, is well justified.

In our earlier model calculations, in which step bunching was not considered, and step field overlap due to both diffusion in the solution *and* on the interface were lumped into $kp(n)$, we used $k=3000$ and $b_{\rm step}=2.72\times10^{-4}$ cm/s [18]. These parameters resulted in quantitative agreement between calculated and experimental local slope variations in response to the macroscopic nonuniformity in interfacial supersaturation [17,18]. However, in preliminary evaluations of the current model we found that step bunching enhances the response of the time-averaged local slope to the nonuniformity in σ^s. Hence, for the base cases in the present simulations we use $k=500$. Since experiments yield the ratio $b_{\rm step}/k$ only, to match the step velocities to the experimentally observed values [8], we reduced $b_{\rm step}$ to 6×10^{-5} cm/s. To investigate the effects of step kinetics nonlinearity on the step bunch dynamics, we used k values of 1000 (increased step interaction), and $k=0$ (no step surface field overlap, linear dependence of step velocity on local interfacial super-

saturation). The values of b_{step} employed in these simulations were 1.2×10^{-4} cm/s and 1.7×10^{-5} cm/s, respectively.

Growth on a facet ceases when all initially imposed steps have reached the center and the facet has become singular; that is, growth can only be sustained through the replenishment of growth steps. Hence, in accordance with recent findings for lysozyme [8,17], we assume that, at the σs used in our simulations, growth steps are generated by 2D nucleation at the edge of the crystal, where the supersaturation is the highest [18,21–23].

The probability P_0 that a nucleus is formed during a simulation time step Δt in a segment of the interface of length Δx with local supersaturation σ^s is proportional to

$$P_0 \propto J_{st}\Delta x\Delta t=[A'\rho_1\exp(-B/\sigma^s)]\Delta x\Delta t, \tag{5a}$$

$$P_0=A\rho_1\exp(-B/\sigma^s), \tag{5b}$$

where J_{st} is the steady-state 2D nucleation rate [24,25], the constant A' contains activation and surface energies as well as frequency factors [25–27], and $B=\pi\Omega\gamma^2h/(k_BT)^2$, with $\Omega=3\times10^{-20}$ cm^3 the volume of a lysozyme molecule in the crystal [15,28], $\gamma=1$ erg/cm^2 the step free energy [9,29], and k_B the Boltzmann constant. At 12 °C ($T=285$ K), this results in $B=67.2$. The value of the constant A is set as follows.

The probability for the generation of a new growth step within a time t_{nucl} after the creation of the previous nucleus or step can be expressed as [30]

$$P(t_{\text{nucl}})=1-\exp[-(t_{\text{nucl}}/\Delta t)P_0]. \tag{6}$$

In the calculations we set the constant A such that the average nucleation time at the initial supersaturation is about h divided by the average normal growth rate R; which for $R=23$ Å/s [3,8] is about 4.7 s. This results in $A=1.65\times10^4$ ml/mg.

We use two modes of step generation. In the *stochastic* mode, $P(t_{\text{nucl}})$ is computed and compared at each time step with a random number $0\leqslant r\leqslant1$. When $r\leqslant P(t_{\text{nucl}})$, a new step is formed and t_{nucl} set to zero. For $r>P(t_{\text{nucl}})$, t_{nucl} is increased by Δt. For a meaningful comparison between the different cases simulated using this step generation mode, the same sequence of 36 000 random numbers was used. In the *deterministic* mode, a step is generated whenever $P_0/P\leqslant\varepsilon$ is satisfied. We set $\varepsilon=0.005$, which results in an initial nucleation rate comparable to that in the stochastic mode.

III. NUMERICAL APPROACH

The time-dependent diffusion equation, Eq. (1), is solved using the same implicit, finite volume approach as in [18,21]. Figure 1(a) illustrates the nonuniform 45×21 global grid (superscript g) used in the simulations of the bulk transport. This grid is based on our earlier simulations of transport in this geometry [18,21]. To accurately resolve the macroscopic interfacial concentration gradients, the first grid point spacing (mesh width) above the top interface, Δz^g, and to the left of the crystal, Δx^g, are both set to 25 μm. Finer grids yield essentially the same global concentration distribution.

To resolve the concentration field about individual growth steps propagating on the vicinal interface, we solve Eq. (1), subject to Eq. (2), also in a mesoscale (MS) subdomain. The 1221×21 grid used in this subdomain for the simulation of transport about the microscopic growth steps is schematically depicted in Fig. 1(b). Note that the outer boundaries of the MS domain coincide with the first mesh lines within the global grid. For the 21 vertical meshes between the crystal corner and the left boundary of the MS domain $N_{\text{sink}}(i)$ in Eq. (3) is zero. The remaining 1200 equally spaced grid points on the interface result in $\Delta x^{\text{MS}}=0.25$ μm; see Eq. (3).

During unsteady growth, steps can move with v's of up to several μm/s; see Sec. VI and [3]. To limit the displacement of even such ''spurting'' steps during a simulation time step Δt to less than Δx^{MS}, we chose $\Delta t=0.025$ s. This assures full utilization of the MS grid for resolving the changes in concentration due to step (sink) motion. Furthermore, during this Δt, the characteristic diffusion distance $\delta_{\Delta t}\approx(D_1\Delta t)^{1/2}\approx1.6$ μm. Hence, the concentration along the two outer boundaries of the mesoscale domain, i.e., 25 μm above and to the left of the crystal (Fig. 1) can be considered fixed during a simulation time step.

To obtain adequate resolution in the MS concentration field normal to the interface, a nonuniform mesh is used in the z direction. It is generated according to

$$\Delta z_i^{\text{MS}}=(25\ \ \mu\text{m})\left[\left(\frac{i}{20}\right)^a-\left(\frac{i-1}{20}\right)^a\right], \tag{7}$$

which with $a=1.8$ results in the mesh width increase from $\Delta z_1^{\text{MS}}=0.11$ μm (i.e., about 10 step heights) at the interface to $\Delta z_{20}^{\text{MS}}=2.2$ μm at the upper boundary of the MS domain.

Step generation and propagation are simulated as follows. When a new step is generated (see Sec. II B), the old steps are renumbered by substituting $n+1$ for n. When a step reaches the facet center, it is annihilated. The step positions are moved along the continuous coordinate x at discrete time intervals according to

$$x_{j+1}(n)=x_j(n)+v_j(n)\Delta t, \tag{8}$$

where the index $j,j+1,...$ represents the specific time step. The step velocity, see Sec. II B, is such that 20–30 Δt's elapse before a step passes through a cell of width Δx^{MS}.

The interstep distances of a set of growth step positions $\{x_j(n)\}$ are

$$d_j(n)=x_j(n+1)-x_j(n). \tag{9}$$

The vicinal slopes p are calculated according to

$$p_j(n)=h/d_j(n). \tag{10}$$

Hence, for a total number of N steps, there are $N-1$ local slopes and growth rates. To account for the competition for nutrient between a growth step and its nearest neighbors on both sides, we used, somewhat arbitrarily, an effective slope

$$p_j'(n)=0.5[p_j(n-1)+p_j(n)] \tag{11}$$

in the evaluation of Eq. (4). Although Eqs. (4) and (11) represent simplifications, we do not expect more realistic formulations for the competition between steps through their surface diffusion fields to result in qualitative modifications of our results.

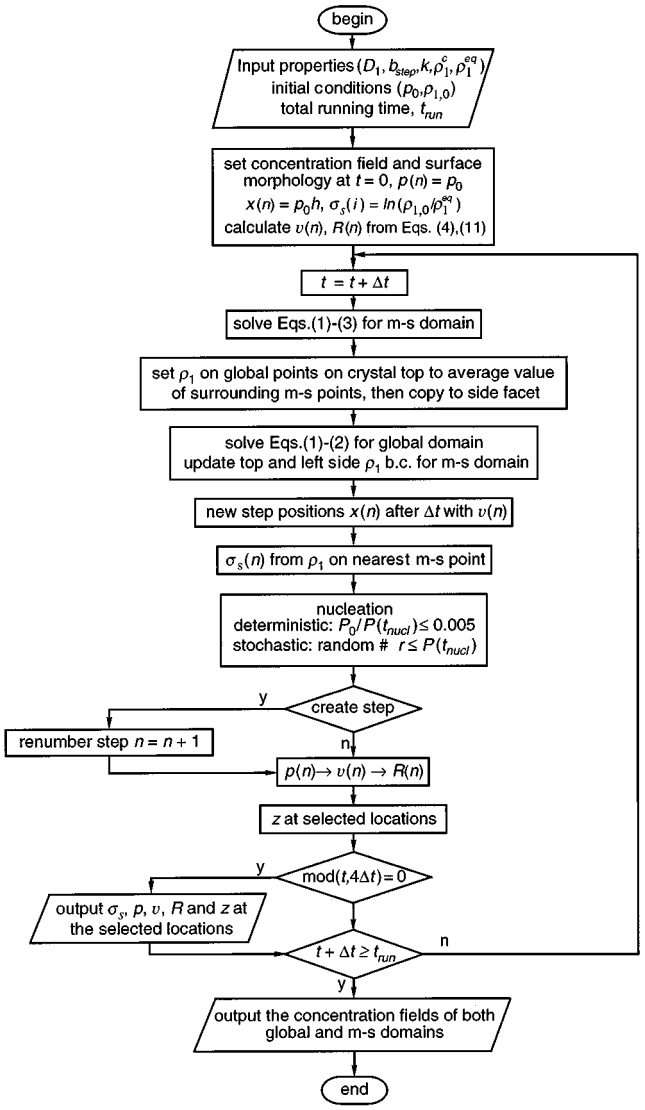

FIG. 2. Flow chart of the simulation steps.

Another simplifying assumption related to Eqs. (4) and (11) concerns the maximum reduction in v due to close step spacing. Note that according to Eq. (4), when $p(n)$ becomes, for instance, 0.2, v is reduced 100-fold. However, in real systems, steps separated by molecular dimensions can move with same order of magnitude velocities as more widely spaced steps [31–33]. Hence, we consider, again somewhat arbitrarily, two steps with interstep distance $\leqslant 5h$, as one step of double height, and replace h in Eq. (3) by $2h$.

The local normal growth rate R is calculated according to

$$R_j(n) = p_j(n) v_j(n). \tag{12}$$

IV. SIMULATION PROCEDURE

The simulation procedure is summarized in Fig. 2. Following input of the system properties $(D_1, \rho_1^c, \rho_1^{eq}, k, b_{step})$ and initial conditions $(\rho_{1,0}, p_0)$ as well as the total running time $t_{run} = \Delta t \times$(number of time steps), the positions of the initially equidistant growth steps, and the initially uniform supersaturation and step velocity are calculated. Then, while keeping the concentration at its outer boundaries fixed, the concentration distribution in the MS domain, that results after a time step in response to the solute flux into the interface, is computed from Eqs. (1)–(3). The concentrations at the global grid points in the horizontal interface [full circles in Fig. 1(b)] are set to the average value of the MS grid points that lie within $\pm \Delta x^g/2$ of the respective global nodes. This interfacial $\rho_1^s(x)$ is also copied onto the interface on the side of the crystal. While holding this new interfacial concentration distribution fixed, the local concentration in the global domain is calculated from Eqs. (1) and (2). This updates the ρ_1 values at the global grid points in the outer boundary of the MS domain [open circles in Fig. 1(b)]. The concentrations at the MS grid points between the global points of this outer boundary are then reset through linear interpolation between the corresponding new global values.

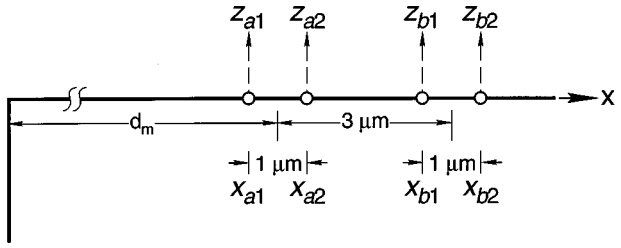

FIG. 3. Definition sketch for averaging used to match the output of simulations with stochastic step generation to the limited spatial resolution of corresponding experiments.

At the end of a time step the new step positions, local slopes and step velocities are calculated from Eqs. (8)–(10) and Eq. (4). Using the new supersaturation at the crystal corner, the nucleation probability is evaluated from Eqs. (5) and (6). After possible creation of a step, all other steps are renumbered. This completes the set of initial condition for the next iteration in the MS domain. The consecutive iterations in the MS and global domains are continued until $t = t_{run}$.

V. DATA PRESENTATION

A. Comparison with experiment

Initially, using stochastic step generation, we obtain time histories of R, p, and v at certain interfacial locations $x = d_m$ measured from the crystal corner. To match the spatial and temporal resolution of the presentation as closely as possible to the experiments [3,10], we proceed as follows. As indicated in Fig. 3, we consider two pairs of points in the vicinity of the location d_m. In both pairs the points are spaced 1 μm apart. This corresponds to the lateral resolution limit given by the pixels in the charge coupled device (CCD) camera used in the experiments [10]. One pair, with positions x_{a1} and x_{a2}, straddles $x = d_m$. The other pair, with positions x_{b1} and x_{b2}, straddles $x = d_m + 3$ μm. This spacing of the pairs corresponds to the pixel spacing used for slope determinations in the experiments. When a step passes through one of these four points, the surface height z at that point is increased by h. This results in local heights z_{a1}, z_{a2}, z_{b1}, and z_{b2}; see Fig. 3. To simulate the lateral averaging due to the finite pixel size, these four values are reduced to two through

$$z_a=\frac{z_{a1}+z_{a2}}{2} \quad \text{and} \quad z_b=\frac{z_{b1}+z_{b2}}{2}. \tag{13}$$

These averaged coordinates are stored at every fourth time step, i.e., every 0.1 s. To simulate the experimental data acquisition time, the z_a and z_b data sets are resampled at 6 s intervals. Then the R, p, and v values are calculated in two ways: (a) To visualize the dynamics of the individual steps, that underlies the macroscopic observations, we calculate from the resampled z_a and z_b data

$$R(t)=\frac{z_a(t)-z_a(t-6\ \text{s})}{6\ \text{s}} \quad \text{and} \quad p(t)=\frac{z_a(t)-z_b(t)}{3\ \mu\text{m}}. \tag{14}$$

(b) To simulate the processing procedures that the experimental data are subjected to [3], the z_a and z_b data sets are converted to intensity values, as they would result from interferometry on the interface, according to

$$I_a=I_1+I_2\cos[2\pi z_b/\Delta_{\text{int}}z],$$

$$I_b=I_1+I_2\cos[2\pi z_b/\Delta_{\text{int}}z], \tag{15}$$

where I_1 and I_2 are arbitrary intensity values, and $\Delta_{\text{int}}z=0.2329$ μm is half the wavelength, in the solution, of the laser illumination used in the interferometry setup [10]. To account for the limited depth resolution of about 200 Å in the experiments, we superimpose a random noise with amplitude corresponding to $\pm h$. Then the simulated intensity traces are processed using the same Fourier signal filtering algorithm as for the actual experimental data [10]. The resulting R- and p-time traces are plotted. Results obtained without random noise addition prior to filtering are very similar, but the higher frequency fluctuations have somewhat lower amplitudes.

B. Analysis of step-bunching mechanism

To elucidate the step-bunching mechanism, we outputted simulation results for layer generation in the deterministic mode. We plotted time traces of p as obtained every 0.1 s at various locations d_m. These presentations were supplemented by spatial profiles of the interface, $z(x)$, and interfacial supersaturation distributions, $\sigma^s(x)$, obtained at select simulation times. In addition, two-dimensional concentration distributions $\rho_1(x,z)$ in the vicinity of steps were obtained from the concentration values on the MS grid.

VI. RESULTS AND DISCUSSION

A. Comparison with experimental results

Results for $R(t)$ and $p(t)$ obtained in the middle of the half facet ($d_m=150$ μm), using the stochastic nucleation mode, the diffusivity of lysozyme and a step interaction parameter $k=500$ are shown in Fig. 4. The points in Fig. 4(a) represent values calculated according to Eqs. (14). Growth rates of 18 and 36 Å/s indicate the passage of one and two growth steps, respectively, through both x_{a1} and x_{a2} during the sampling interval. R values of 9 and 27 Å/s indicate that one of the steps that passed through x_{a1} has not reached x_{a2} during the 6 s. Similarly, the p values of 3.6×10^{-3} and its

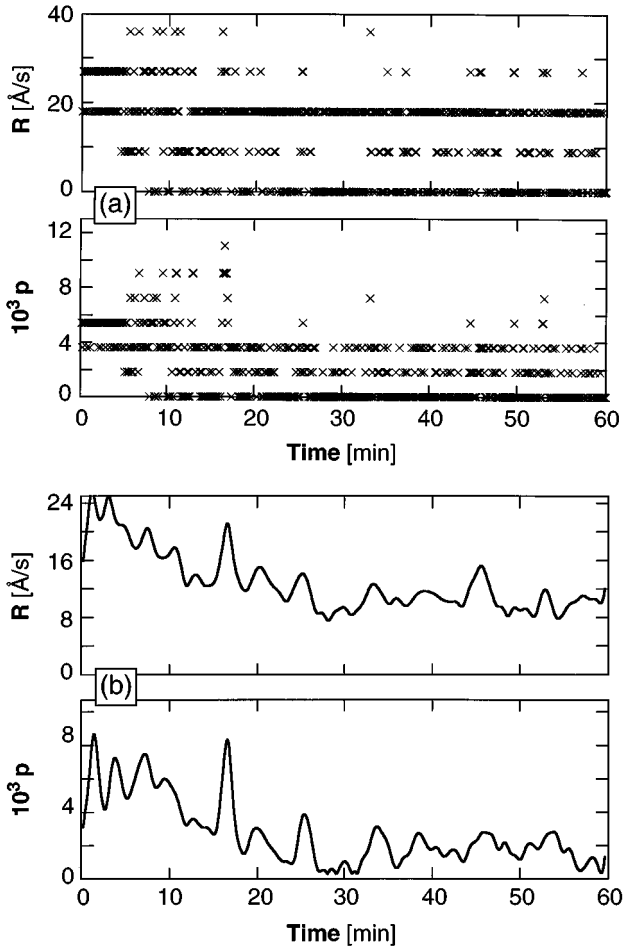

FIG. 4. Growth rate $R(t)$ and slope $p(t)$ obtained in the stochastic nucleation mode with $k=500$ and $D=D_{\text{lysozyme}}$ at the middle of the half facet; (a) before and (b) after data processing to reduce spatial resolution to those of our experiments [3,10].

multiples indicate that at the sampling time the number of steps between x_{a1} and x_{a2} differs from the number of steps between x_{b1} and x_{b2} by an even number. The p values of 1.8×10^{-3} and odd multiples indicate that this difference is an odd number.

Figure 4(b) shows the same results after processing of the full data sets to account for the limited spatial resolution of the experiments; see Sec. V A. First we note that in contrast to the experimental results, see Fig. 5 and [3], both the average growth rate and slope obtained from the simulation systematically decrease. This is due to the larger ratio of crystal ''surface area'' to solution ''volume'' in the 2D simulation model. As a consequence, the bulk supersaturation in the model decreases more rapidly than in the experiment.

From the $p(t)$ trace in Fig. 4(b) one sees that the growth rate fluctuations are due to the passing of step bunches. The characteristic time between the passage of major step bunches is several minutes. This is about two orders of magnitude longer than the average step generation (nucleation) time of $\sim$5 s.

To facilitate their quantitative comparison, we have decomposed the simulated and experimental $R(t)$ of Fig. 4(b) and Fig. 5, respectively, into their Fourier components; see

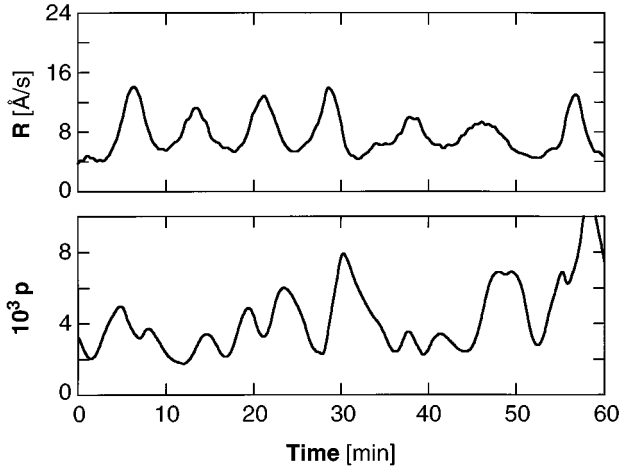

FIG. 5. Experimental results obtained with lysozyme at $\sigma=2.84$ and $T=12$ °C; from [3].

Fig. 6. To correct for the model-induced decrease in average growth rate, we disregard the four lowest frequency components; see the dashed lines in Fig. 6(a). The inset in Fig. 6(a) shows $R(t)$ after deduction of these lowest components, together with a trace resulting from the superposition of these components alone. In comparing Figs. 6(a) and 6(b) we see that the simulation reproduces both the amplitude and characteristic time of the R fluctuations observed in the experiments rather well.

B. Effects of bulk transport and step kinetics nonlinearity

To test our earlier supposition [3] that the fluctuation amplitude depends on both the nonlinearity of the interfacial kinetics and the relative importance of bulk transport and

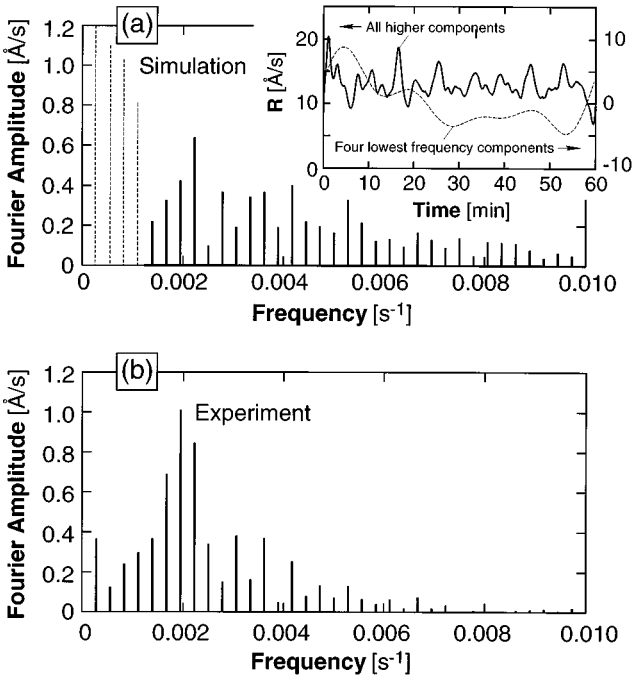

FIG. 6. Fourier decomposition of $R(t)$. (a) Simulation results (Fig. 4); inset: subtraction of four lowest frequency components of $R(t)$, for details see text. (b) Experimental results (Fig. 5).

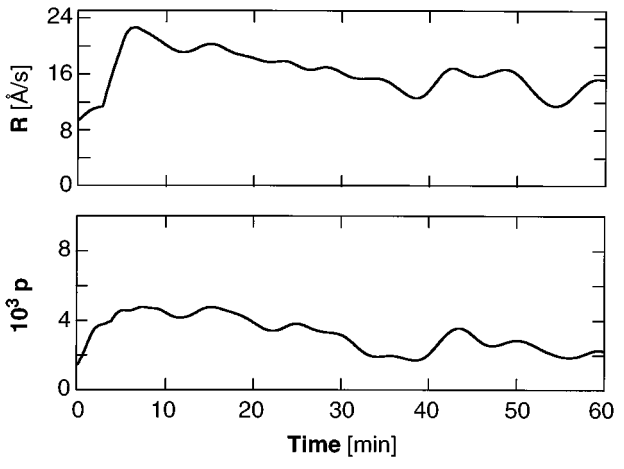

FIG. 7. Growth rate $R(t)$ and slope $p(t)$ obtained in the stochastic nucleation mode with $k=500$ and $D=10D_{\text{lysozyme}}$ (after data processing) at the middle of the half facet.

interface kinetics, we have varied the model input parameters. Figure 7 presents the result of a simulation with all parameters the same as for Fig. 4, except for a tenfold increase in D_1. Comparing Figs. 7 and 4(b) we see that this shift towards kinetics control drastically reduces the fluctuation amplitude.

To illustrate the role of the step surface interaction parameter k, we returned to our base case of Fig. 4 (i.e., with D_1) and set $k=0$. Thus, in this simulation, nonlinearity in step kinetics is only due to overlap of the steps' bulk diffusion fields [31,33–35] and step generation through (stochastic) nucleation. Figure 8 shows that the R and p fluctuations are weaker than in Fig. 4(b). Apparently, the nonlinearity resulting from the step generation process suffices for the development of the remaining long-term fluctuations. In Sec. VI F we will see that the key nonlinearity lies in the stochastic nature of the step generation. In simulations with deterministic step generation but otherwise identical assumptions, practically no fluctuations were obtained.

These results unambiguously confirm our expectation that, similar to the unsteady behavior of other systems in-

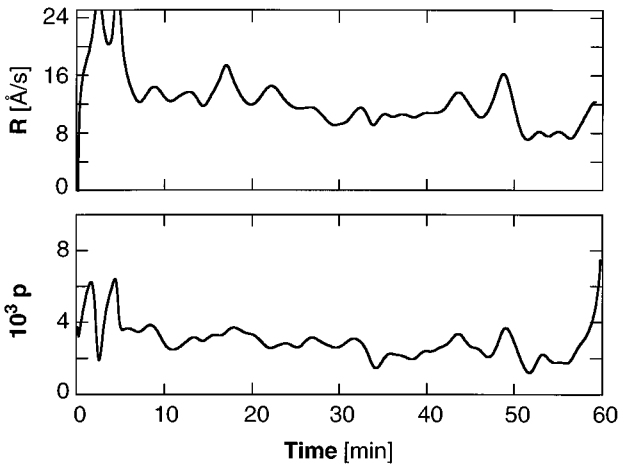

FIG. 8. Growth rate $R(t)$ and slope $p(t)$ obtained in the stochastic nucleation mode with $k=0$ and $D=D_{\text{lysozyme}}$ (after data processing) at the middle of the half facet.

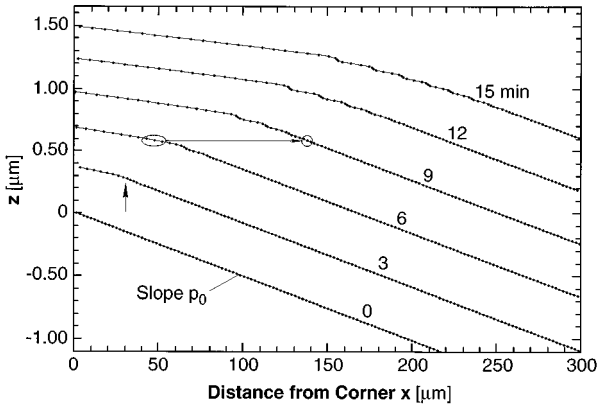

FIG. 9. Interface profiles obtained at various simulation times in the deterministic nucleation mode with $k=500$ and $D=D_{\text{lysozyme}}$. Changes in z values at $x=0$ account for layers generated between times noted, i.e., individual steps propagating inwards on facet retain equal z. Horizontal arrow illustrates passage of individual steps through step bunches. Vertical arrow points at initial slope perturbation that triggers the bunch cascade seen in later profiles.

volving coupled bulk transport and nonlinear kinetics [36–38], both the nonlinearity in growth step kinetics and mixed transport-kinetics control of the crystallization process are necessary conditions for the growth rate fluctuations.

C. Phenomenology of step bunching

Stochastic nucleation obscures the details of interaction between transport to the interface and step motion. To gain insight into the microscopic mechanism underlying the growth rate fluctuations, we removed the random element in the step generation by using the deterministic nucleation mode for all following simulations.

Figure 9 shows a temporal sequence of interface profiles obtained for otherwise same conditions as those for Fig. 4. Each point corresponds to a single step. The contour for $t=0$ represents the initially equidistant step train corresponding to $p_0=5\times10^{-3}$. Consecutive contours are plotted such that individual steps propagating inwards on the facet retain the same z coordinate throughout this sequence. Hence, the changes in z values between consecutive contours account for the growth between the times noted. This sequence of interface profiles reveals that growth is associated with a morphological adjustment over the whole vicinal face: New steps are generated, according to the supersaturation at the facet corner, at a lower rate than is required to maintain the initial p_0. This causes a kink in step density (see the arrow on the 3 min profile in Fig. 9) which moves toward the middle of the facet. During this inward motion, a step bunch of continuously increasing local slope evolves from this kink. Simultaneously, a cascade of new bunches forms ahead of the first one, which steepen as they move toward the facet center. For the discussion of possible capillary effects in Sec. II B it is important to note that the smallest radius of interfacial curvature associated with these step bunches is of the order of 100 μm, i.e., four orders of magnitude larger than the capillary length of this system.

The evolution of these step bunches can be followed over the whole simulation period in Fig. 10, which presents time traces of the slope at the three locations ($d_m=15$, 150, and 285 μm) schematically indicated in the insets. As expected from Fig. 9, one sees that the number and magnitude of the maxima, which represent the passage of step bunches, depend on the sampling location. Close to the crystal edge, p decreases rather monotonically from the initial $p_0=5\times10^{-3}$ to 1×10^{-3}. In the middle of the half facet, however, $p(t)$ shows several spikes of successively increasing amplitude and spacing. Close to the facet center, the number, size and spacing further increase. The fine spikes, superimposed on the larger ones, indicate the passage of individual growth steps of height h. They become apparent only in such a group of closely spaced steps, since we calculate p from the distances between nearest steps. By comparison with Fig. 9 we see that the steepest bunch, which arrives last at a given location, is the one that originated from the initial kink in step density. All other peaks, that arrive earlier, represent bunches which formed in front of the first one at later times.

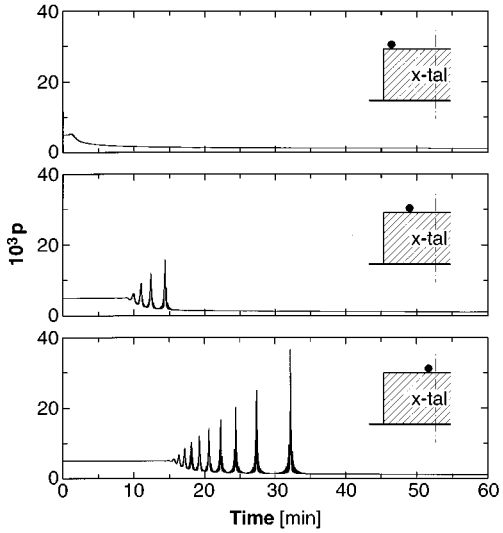

FIG. 10. Time traces of slope p obtained in the deterministic nucleation mode with $k=500$ and $D=D_{\text{lysozyme}}$, at the three interface locations $d_m=15$ μm, 150 μm, and 285 μm. Large spikes indicate passage of step bunches; small spikes, passage of individual steps.

In Sec. VI D we will show that this steepening and cascading of step bunches results from a more complex mechanism than that underlying the kinematic wave descriptions of the evolution of a single step bunch [39,40]. Yet, it is interesting to find that the original kinematic wave concept can account for some of the features of the simulation results. Most importantly, as anticipated in [39,40], the elementary steps move through the slower traveling bunches. This is illustrated, for instance, by the arrow connecting the group of three advancing steps in the 6 and 9 min profiles of Fig. 9. While the velocity of all bunches, as evaluated from these plots, is about $v_{\text{bunch}}\approx0.16$ μm/s, the individual steps travel with $v\approx0.5$ μm/s in the same direction. Using the kinematic wave velocity as defined in [39],

$$v_{\text{wave}}=\frac{\partial R}{\partial p}, \tag{16}$$

we can write for the velocity of a bunch, using Eqs. (4) and (12),

$$v_{\text{bunch}}=\left.\frac{\partial R}{\partial p}\right|_{\text{bunch}}=\left.\frac{b_{\text{step}}\sigma^s}{(1+kp)^2}\right|_{\text{bunch}}=\left.\frac{v}{1+kp}\right|_{\text{bunch}}. \quad (17)$$

For the above $k=500$ and $p=5\times10^{-3}$, Eq. (17) yields $v/v_{\text{bunch}}=3.5$, in reasonable agreement with the above simulation result. Furthermore, kinematic wave theory predicts that the number of steps in a bunch does not change *en route* across a facet. Figure 9 shows that all bunches consist of the same number of individual steps, irrespective of a bunch's steepness and position.

Recently, step bunching, with and without solution flow, has been analyzed in terms of linear stability theory, assuming step interaction in the bunch through the bulk diffusion fields only [41–44]. The velocity of step bunches, that form in crystallization from solutions under diffusive transport conditions, has been related to the velocity of the individual steps by [42]

$$v_{\text{bunch}}=v\left(1+\frac{b_{\text{step}}\overline{p}}{Dk_x}\right)^{-1}. \quad (18)$$

Here $\overline{p}$ is the macroscopic slope of the vicinal face and k_x is the wave number of the step bunch (harmonic perturbation in step density) parallel to the interface. Evaluation of Eq. (18) with the previously introduced parameters for lysozyme and $k_x=0.4\ \mu\text{m}^{-1}$ (corresponding to an approximate wavelength of 15 μm deduced from Fig. 9) results in $b_{\text{step}}\overline{p}/Dk_x\approx10^{-4}$. Thus, in contrast to the above findings, Eq. (18) predicts $v_{\text{bunch}}\approx v$. This further emphasizes that the step bunching mechanism observed in our work differs from the linear morphological instabilities obtained in [42–44].

Note that in Fig. 9, after readjustment of the interface shape to the growth-induced nonuniformity in interfacial supersaturation [17,18,21,45,46], step bunching ceases. Yet, in the experiments, and the simulations with stochastic step generation, fluctuations prevail as long as growth occurs. This can be understood in terms of the intrinsically unsteady nature of growth step sources. Dislocation groups typically produce step trains with varying interstep distance [31,47–49]. Similarly, 2D nucleation sources produce steps in stochastic sequence. Hence, both step generation mechanisms are prone to incessantly produce morphological perturbations in the form of local slope variations. While moving across the facet, these slope nonuniformities readjust their step spacing to the prevailing transport and kinetics conditions. As we will see in more detail below, nonlinearities in kinetics can lead to a new step bunching cascade each time the source creates such a perturbation.

D. Nutrient supply and dynamics of step-bunch cascading

Insight into the dynamics of the above step bunching and cascading can be obtained from correlations of the interface morphology to underlying concentration and supersaturation distributions. Figure 11 presents the evolution of a section of the interface in higher spatial resolution and for shorter time increments than Fig. 9. The corresponding interfacial supersaturation profiles $\sigma^s(x)$ are given in Fig. 12. The overall slope of the $\sigma^s(x)$ curves reflects the monotonic decrease in supersaturation from the edge to the center of facets of growing crystals [18,21–23]. Negative spikes are superimposed

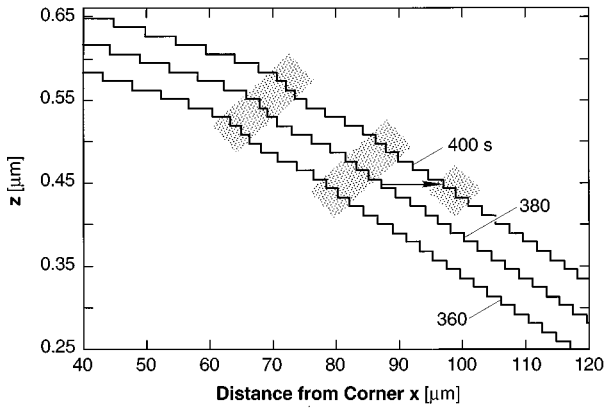

FIG. 11. High-resolution interfacial profiles for conditions of Fig. 9. The 360 s profile is the central section of the 6 min profile in Fig. 9. Shaded areas indicate step bunches. Arrow illustrates the accelerated departure of the leading step of a bunch to form new bunch ahead of old one.

on this monotonic drop-off. By overlaying Figs. 11 and 12, one recognizes that these spikes are located at the steps. One also sees that at the location of step bunches (shaded areas in Fig. 11) the spike pattern in $\sigma^s(x)$ is modulated. As emphasized in the magnified part of the 360 s trace in Fig. 12, the supersaturation values between and at the steps in a bunch are, respectively, lower and higher than the values expected for equidistant steps at the same location. The lower values at the step bunches reflect the higher local step (sink) density; see Eq. (3). The higher values at the individual steps in a bunch (see also Fig. 13 for the σ^s values at all step locations of Fig. 9) are a consequence of the reduction in solute consumption rate *per step* due to the closer step spacing; see Eq. (4). The corresponding reduction of the concentration gradient at a step bunch, in both the x and z directions, is further illustrated by the isoconcentration lines, $\rho_1(x,z)$ in Fig. 14.

Now we are in a position to elucidate the step bunch formation and cascading mechanism in detail. As indicated

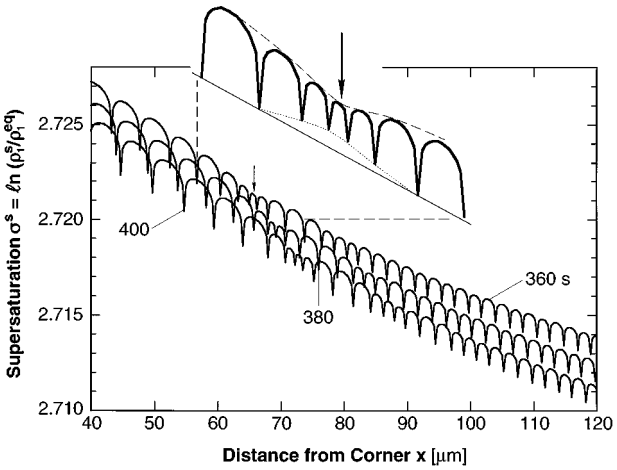

FIG. 12. High-resolution interfacial supersaturation profiles corresponding to Fig. 11. Inset: magnified section of the 360 s profile with step bunch about the arrow. Note the increase of σ^s *at* the steps of a bunch (dotted line), decrease of σ^s over the bunch (dashed line) compared to σ^s for equidistant step train (thin solid line).

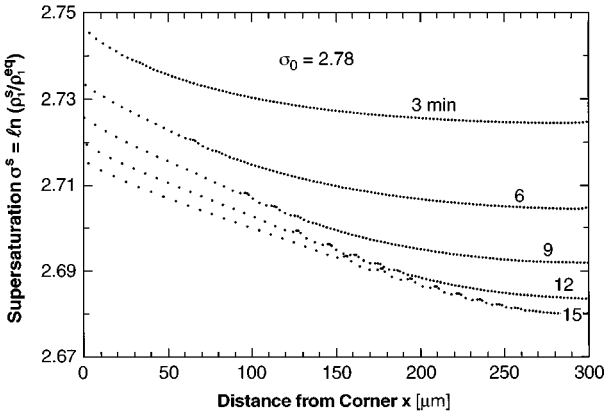

FIG. 13. Supersaturations at the step locations of Fig. 9.

in the preceding section, the first bunch forms at the initial kink in step density; see the vertical arrow at the 3 min profile in Fig. 9. In passing through this kink, due to less competition from the rear, a step is better supplied than the steps ahead of it. Hence, it catches up with them and forms a bunch. Bunching, as discussed above, is accompanied by an increase in σ^s at the steps of the bunch. Note that the envelope of the increased σ^s values (dotted line in the inset of Fig. 12) is akin of the supersaturation that the steps encounter *en route* through the bunch. As a consequence, steps moving through a bunch, in particular the leading step which experiences less competition from the nearest, wider spaced step outside the bunch, can catch up with the steps in front of them (see arrow in Fig. 11). This initiates the formation of a new bunch ahead of the already existing one.

The bunch cascading and steepening can also be understood in terms of an expansion of the kinematic wave theory (KWT) [39]. In its original version, the KWT of step bunching is based on the premise that the v_{wave} depends only on the step density, that is, on p. Thus, the bunch cascading observed in this work is not predicted in [39], and a continuous increase in bunch steepness is found only under the action of impurities [39,40,50,51]. However, as we have seen in connection with Eq. (17), in our system, v_{wave} is also a function of interfacial supersaturation. In the following we will accommodate this dependence.

Differentiating Eq. (17) with respect to p we get

$$\frac{\partial v_{\text{bunch}}}{\partial p} = -\frac{2kb_{\text{step}}\sigma^s}{(1+kp)^3} < 0. \tag{19}$$

As a bunch moves towards the facet center, σ^s decreases due to both the global gradient and the protein depletion in the

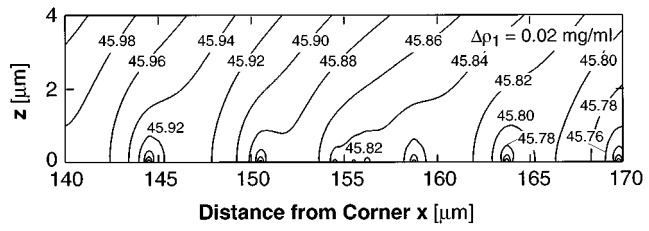

FIG. 14. High-resolution concentration distribution, $\rho_1(x,z)$, in midsection of the 15 min profile of Fig. 9. Note reduction of gradients around step bunch (three steps) at $\approx$155 μm.

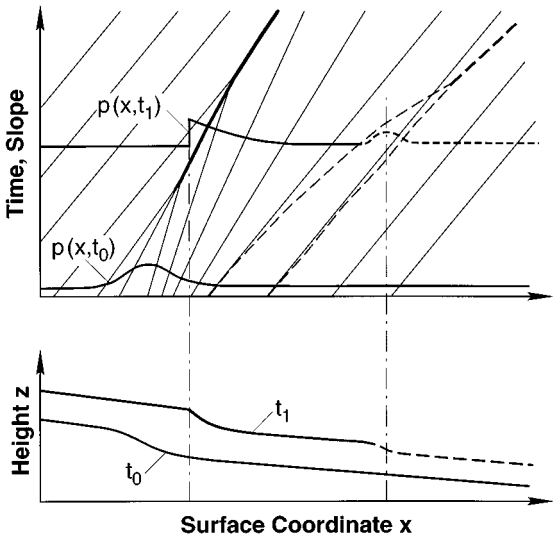

FIG. 15. Expansion of kinematic wave model. Progressive displacement and change of shape of step bunch. Straight lines: characteristics resulting from kinematic wave theory; dashed lines: modification due to dependence of v_{wave} on supersaturation. Growth steps move from left to right. For details see text.

closed system (see Sec. VI A). As a consequence v_{bunch} decreases *en route*; see Eq. (17). Since, according to Eq. (19), $\partial v_{\text{bunch}}/\partial p$ is negative, the continuous reduction in v_{bunch} is accompanied by steepening of the bunch. As in step motion against a spatial supersaturation gradient [17,18], this effect is strongly amplified by the decelerating interstep interaction, so that a σ_{step} decrease from 2.715 to 2.68 (Fig. 13) results in an increase in bunch slope by an order of magnitude (Fig. 10).

For discussing the bunch cascading within the framework of the KWT, we present in Fig. 15 a modification of Fig. 4 of [39]. Note that the original figure illustrates dissolution rather than growth. According to the KWT, if, as originally assumed, v_{wave} depends on p only, each section of a step train evolves along straight characteristic lines in the (p,x,t) space. The slope of the projections of these characteristics into the (x,t) plane is inversely proportional to v_{wave} defined in Eq. (16). With $\partial v_{\text{bunch}}/\partial p < 0$ from Eq. (19), the higher the p of a section of the step train, the steeper is its characteristics. Hence, as schematically indicated in Fig. 15, whatever the initial profile in a bunch, on its way across a facet it will develop a discontinuity of slope at the rear and become increasingly rounded at the front. Steps outside a bunch travel with constant v_{wave} and are, thus represented by parallel characteristics, implying that no new bunches form.

In our case, as we have discussed in connection with Fig. 12, step bunching results in increased supersaturation at the steps in the bunch. Hence, as can be deduced from Eq. (17), v_{wave} increases most at the bunch's head, where p is lowest within the bunch. Thus, as indicated by the dashed curve in the (x,t) plane in Fig. 15, the slope of the characteristics of this section of the step train will continuously decrease. This will lead to the appearance of a new step bunch ahead of the existing one, at the location of intersection of this curved characteristics with another less curved one.

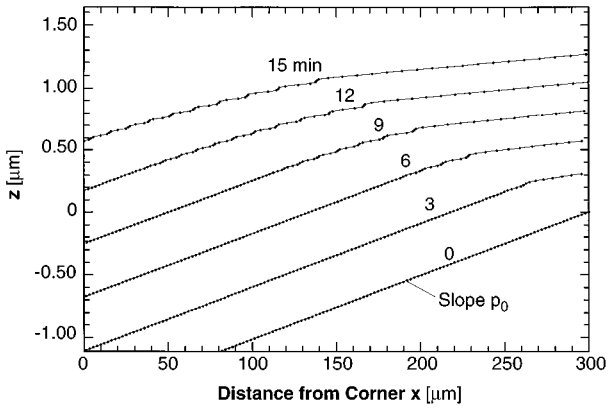

FIG. 16. Interface profiles obtained for outward motion of steps at various simulation times in the deterministic nucleation mode with $k=500$ and $D=D_{\text{lysozyme}}$.

E. Step motion in the direction of the global interfacial supersaturation gradient

The wavelike evolution of step bunches is not limited to step motion from a facet edge to its center. Figures 16 and 17 present the results of a simulation identical to that underlying Figs. 9–14, except that steps are generated at the facet center and move towards the crystal edge. The $z(x)$ profiles reveal again a step bunching cascade associated with the morphological transition. The corresponding $p(t)$ traces in Fig. 18 show that the magnitude of the p maxima is comparable to those obtained in the case of the inward motion of the steps. However, the number of bunches is increased and their spacing is slightly decreased. Furthermore, in comparing the 3 and 6 min profiles in Figs. 16 and 17 to those in Figs. 9 and 13, we see that step bunching occurs somewhat earlier during the outward step motion.

From a macroscopic point of view, these results appear surprising: Step motion in the direction of the supersaturation gradient results in interfacial supersaturations that are higher at the leading steps than at the trailing steps of a bunch. This should lead to acceleration of the leading steps and deceleration of the trailing ones, and, thus, to debunching. Yet, on a more local scale, there are two effects that counteract debunching. First, during growth through step generation at the facet center, the initial shape perturbation that triggers the bunch cascade is stronger than in the case of

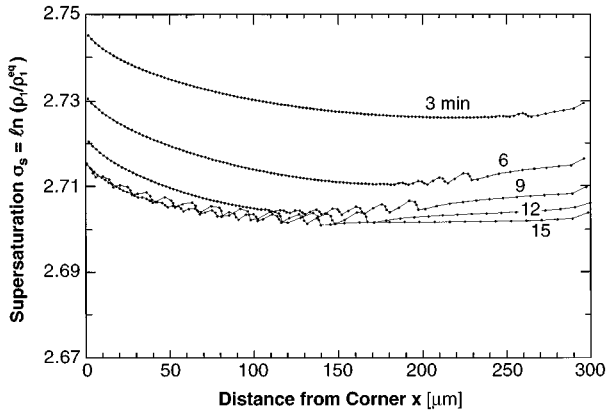

FIG. 17. Supersaturations at steps of Fig. 16.

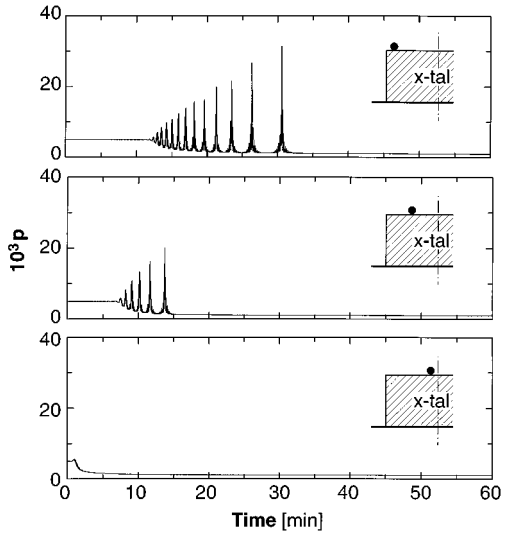

FIG. 18. Time traces of slope p obtained in deterministic nucleation mode for outward moving steps with $k=500$ and $D=D_{\text{lysozyme}}$ at $d_m=15$ μm, 150 μm, and 285 μm.

Figs. 9–14. This is because of the larger difference between p_0 and the low p that results from step generation at the lower supersaturation of the facet center. Second, as surmised above, the bunch cascading is caused by the higher supersaturation, in particular, at the leading edge of a bunch. In this case, both the global gradient in σ^s and the local σ^s increases from bunching cause an increase in supersaturation in front of the leading steps. This causes stronger cascading than in inward step motion.

As another consequence of the mutual enhancement of the global supersaturation gradient and the local σ^s perturbations, the kinematic wave nature of the bunch evolution becomes more apparent. The transition from a symmetric shape of newly formed bunches to the slope discontinuity at the trailing edge in ''older'' ones is well reflected in Fig. 16. Figure 17 shows that this asymmetric bunch morphology is associated with asymmetric peaks in σ^s at the steps of ''older'' step bunches.

This comparison of the inward and outward motion of steps points also at an interesting difference with respect to the morphological stability of facets. Step bunching strongly modifies the response of the interface shape to the global supersaturation gradient. Note that if step bunching is not considered, the lower global supersaturation at the facet center should lead to step retardation and, thus, to a higher local slope. This is expected irrespective of the location of step generation and the direction of step motion, see the discussion in [41]. However, the steepening of the bunches along their path leads to an additional decrease in the time-averaged step velocity. For inward motion of the steps, as in Fig. 9, this results in a stronger nonuniformity in the time-averaged local slope at the facet center. Yet, in outward step motion, this retardation results in a *higher* slope at the facet periphery, see Fig. 16. These effects of the step bunching should have important consequences for the morphological stability of faceted crystals growing from a nonuniform supply field discussed in [45,46,52,53] and references therein.

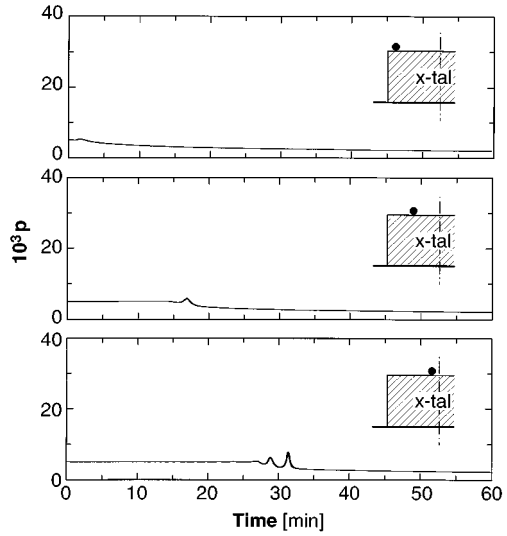

FIG. 19. Time traces of slope p obtained in deterministic nucleation mode for inward moving steps with $k=500$ and $D=10D_{\text{lysozyme}}$.

F. Effects of bulk transport and step kinetics nonlinearity on bunch cascading

To further explore the dependence of the bunch cascading on the relative weight of interfacial kinetics and bulk transport, and on the degree of nonlinearity in kinetics, we have performed simulations identical to the case of Fig. 10, except for changes in the diffusivity D and the step interaction parameter k.

Figure 19 shows $p(t)$ traces obtained with $D=10D_{\text{lysozyme}}$. By comparison with Fig. 10, one sees that in response to this shift towards kinetics control, the fluctuation amplitude is reduced by about one order of magnitude. On the other hand, with D_{lysozyme} an increase in the nonlinearity of kinetics through the doubling of k to 1000 results in significant increases in the amplitude and characteristic time of the fluctuation (Fig. 20). Finally, with $k=0$, the morphology readjustment in our system occurs without step bunching, Fig. 21.

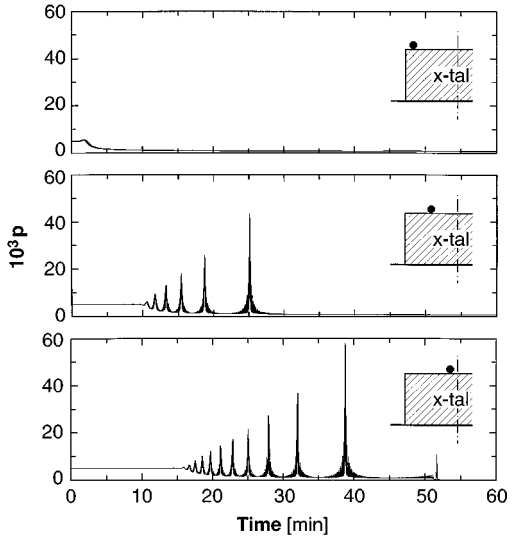

FIG. 20. Time traces of slope p obtained in deterministic nucleation mode for inward moving steps with $k=1000$ and $D=D_{\text{lysozyme}}$.

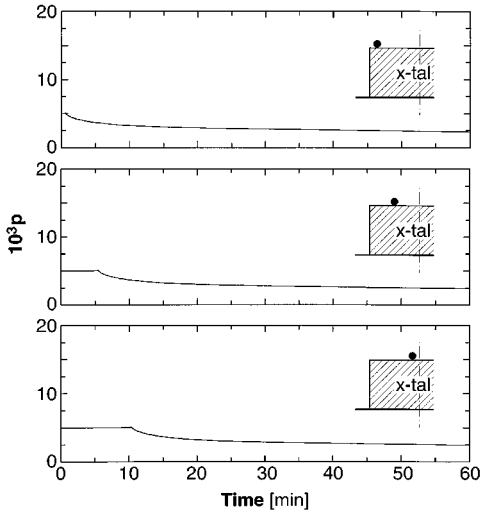

FIG. 21. Time traces of slope p obtained in deterministic nucleation mode for inward moving steps with $k=0$ and $D=D_{\text{lysozyme}}$.

The results of these parameter variations well corroborates our supposition that the fluctuations represent the nonlinear response of the coupled bulk transport and step motion in the mixed control regime [3].

VII. SUMMARY AND CONCLUSIONS

We have developed a numerical model that combines diffusion in the bulk of a solution with diffusive transport to microscopic growth steps that propagate on a finite crystal facet. Nonlinearities in layer growth kinetics arising from step interaction by bulk and surface diffusion, and from step generation by surface nucleation, are taken into account. We have evaluated the model with properties characteristic for the solute transport, step generation and propagation in the lysozyme solution growth system. The model reproduces the time scale and amplitude of the fluctuations in normal growth rate and local slope obtained experimentally. The fluctuation time scale is large compared to that of step generation. The local slope variations indicate that the fluctuations stem from step bunching. Variations of the governing parameters of the model reveal that the step bunching investigated here represents the nonlinear response of the step interaction kinetics to step generation perturbations, under mixed transport-kinetics control. Thus, with stronger kinetics control of growth, the step bunching was practically nonexistent, while stronger step kinetics nonlinearity resulted in more pronounced bunching.

These findings bear considerable practical consequences. Depending on the transport and kinetics parameters of a system, a change of the role of transport through a change in convection can either enhance or reduce unsteadiness in growth. Since the associated step bunching is typically associated with the formation of structural and compositional nonuniformity, such imposed shifts in growth control can be expected to result in system-dependent improvement or degradation in crystal homogeneity.

On a microscopic scale, we found that the fluctuations result from a morphological instability of the vicinal face, in

which a step bunch triggers a cascade of new step bunches through modifications of the interfacial supersaturation distribution. Leading steps in a bunch are accelerated and, on catching up with steps in front of the bunch, form a new bunch. Finally, we have shown that both the continuous steepening of step bunches and the bunch cascading obtained in the simulations can be interpreted in terms of an expanded kinematic wave model.

ACKNOWLEDGMENTS

We thank J. I. D. Alexander for stimulating discussions. This work was supported by NASA (Grants Nos. NAG8-1161 and-1168) and the State of Alabama through the Center for Microgravity and Materials Research at the University of Alabama in Huntsville and the Alabama Supercomputer Network.

[1] F. Rosenberger, *Fundamentals of Crystal Growth, Vol. I: Macroscopic Equilibrium and Transport Concepts* (Springer, Berlin, 1979), p. 450.
[2] A. A. Chernov, *Modern Crystallography, Vol. III: Growth of Crystals* (Springer, Berlin, 1984), p. 246.
[3] P. G. Vekilov, J. I. D. Alexander, and F. Rosenberger, Phys. Rev. E. **54**, 6650 (1996).
[4] J. M. Garcia-Ruiz, A. Santos, and E. J. Alfaro, J. Cryst. Growth **84**, 555 (1987).
[5] P. J. Ortoleva, *Geochemical Self-Organization* (Oxford University Press, New York, 1994).
[6] J. J. Favier, J. Electrochem. Soc. **129**, 2355 (1982).
[7] M. Piechotka, J. Cryst. Growth **146**, 1 (1995).
[8] P. G. Vekilov and F. Rosenberger, J. Cryst. Growth **158**, 540 (1996).
[9] A. A. Chernov and H. Komatsu, in *Science and Technology of Crystal Growth*, edited by J. P. van der Eerden and O. S. L. Bruinsma (Kluwer, Amsterdam, 1995), p. 329.
[10] P. G. Vekilov, L. A. Monaco, and F. Rosenberger, J. Cryst. Growth **148**, 289 (1995).
[11] L. A. Monaco and F. Rosenberger, J. Cryst. Growth **129**, 465 (1993).
[12] F. Rosenberger, S. B. Howard, J. W. Sowers, and T. A. Nyce, J. Cryst. Growth **129**, 1 (1993).
[13] S. B. Dubin, G. Feher, and G. B. Benedek, Biochemistry **12**, 714 (1973).
[14] V. Mikol, E. Hirsch, and R. Giege, J. Biol. Chem. **213**, 187 (1990).
[15] C. C. F. Blake, G. A. Mair, A. C. T. North, D. C. Phillips, and V. R. Sarma, Proc. R. Soc. London Ser. B **167**, 365 (1967).
[16] F. Rosenberger, *Fundamentals of Crystal Growth, Vol. I: Macroscopic Equilibrium and Transport Concepts* (Springer, Berlin, 1979), p. 226.
[17] P. G. Vekilov, L. A. Monaco, and F. Rosenberger, J. Cryst. Growth **156**, 267 (1995).
[18] H. Lin, P. G. Vekilov, and F. Rosenberger, J. Cryst. Growth **158**, 552 (1996).
[19] H. Freundlich, *Colloid and Capillary Chemistry* (Dutton, New York, 1926), p. 154.
[20] A. A. Chernov, *Modern Crystallography, Vol. III: Growth of Crystals* (Springer, Berlin, 1984), p. 49 and p. 6.
[21] H. Lin, F. Rosenberger, J. I. D. Alexander, and A. Nadarajah, J. Cryst. Growth **151**, 153 (1995).
[22] A. Seeger, Philos. Mag. **44**, 348 (1953).
[23] W. R. Wilcox, J. Cryst. Growth **37**, 229 (1977); **38**, 73 (1977).
[24] A. A. Chernov, *Modern Crystallography, Vol. III: Growth of Crystals* (Springer, Berlin, 1984), p. 127.
[25] A. J. Malkin, A. A. Chernov, and I. V. Alexeev, J. Cryst. Growth **97**, 765 (1989).
[26] B. Mutaftschiev, in *Handbook of Crystal Growth. I. Fundamentals Part A: Thermodynamics and Kinetics*, edited by D. T. J. Hurle (North-Holland, Amsterdam, 1993), p. 187.
[27] D. Kashchiev, in *Science and Technology of Crystal Growth*, edited by J. P. van der Eerden and O. S. L. Bruinsma (Kluwer, Dordrecht, 1995), p. 53.
[28] L. K. Steinrauf, Acta Crystallogr. **12**, 77 (1959).
[29] P. G. Vekilov, L. A. Monaco, B. R. Thomas, V. Stojanoff, and F. Rosenberger, Acta Crystallogr. D **52**, 785 (1996).
[30] S. Toshev, A. Milchev, and S. Stoyanov, J. Cryst. Growth **13/14**, 123 (1972).
[31] W. K. Burton, N. Cabrera, and F. C. Frank, Philos. Trans. R. Soc. London Ser. A **243**, 299 (1951).
[32] G. H. Gilmer, R. Ghez, and N. Cabrera, J. Cryst. Growth **8**, 79 (1971).
[33] J. P. van der Eerden, J. Cryst. Growth **56**, 174 (1982).
[34] A. A. Chernov, Usp. Fiz. Nauk **73**, 277 (1961) [Sov. Phys. Usp. **4**, 116 (1961)].
[35] A. A. Chernov, *Modern Crystallography, Vol. III: Growth of Crystals* (Springer, Berlin, 1984), p. 123.
[36] C. J. Allegré, A. Provost, and C. Jaupart, Nature **295**, 223 (1981).
[37] P. Gray and S. K. Scott, *Chemical Oscillations and Instabilities. Non-linear Chemical Kinetics* (Clarendon, Oxford, 1990).
[38] R. M. Noyes and R. J. Fields, Ann. Rev. Phys. Chem. **25**, 95 (1974).
[39] F. C. Frank, in *Growth and Perfection of Crystals*, edited by R. H. Doremus, B. W. Roberts, and D. Turnbull (Chapman and Hill, London, 1958), p. 411.
[40] N. Cabrera and D. A. Vermilyea, in *Growth and Perfection of Crystals*, edited by R. H. Doremus, B. W. Roberts, and D. Turnbull (Chapman and Hill, London, 1958), p. 393.
[41] A. A. Chernov and T. Nishinaga, in *Morphology of Crystals*, edited by I. Sunagawa (Terra, Tokyo, 1987), p. 207.
[42] A. A. Chernov, J. Cryst. Growth **118**, 333 (1992).
[43] A. A. Chernov, S. R. Coriell, and B. T. Murray, J. Cryst. Growth **132**, 405 (1993).
[44] S. R. Coriell, B. T. Murray, A. A. Chernov, and G. B. McFadden, J. Cryst. Growth **169**, 773 (1996).
[45] A. A. Chernov, Kristallografiya **16**, 842 (1971) [Sov. Phys.-Crystallogr. **16**, 734 (1972)].
[46] A. A. Chernov, J. Cryst. Growth **24/25**, 11 (1974).
[47] J. J. DeYoreo, T. A. Land, and B. Dair, Phys. Rev. Lett. **73**, 838 (1994).

[48] K. Onuma, T. Kameyama, and K. Tsukamoto, J. Cryst. Growth **137**, 610 (1994).
[49] A. J. Malkin, Yu. G. Kuznetsov, T. A. Land, J. J. DeYoreo, and A. McPherson, Nature Struct. Biol. **2**, 956 (1995).
[50] J. P. van der Eerden and H. Müller-Krumbhaar, Electrochim. Acta **31**, 1007 (1986).
[51] J. P. van der Eerden and H. Müller-Krumbhaar, Phys. Rev. Lett. **57**, 2431 (1986).
[52] J. W. Cahn, in *Proceedings of the International Conference on Crystal Growth, Boston, 1966*, edited by H. S. Peiser (Pergamon, Oxford, 1967), p. 681.
[53] R. F. Sekerka, J. Cryst. Growth **128**, 1 (1993).